Research Article | Vol. 30, No. 13 / 20 Jun 2022 / Optics Express 23102
Optics EXPRESS

Tunable angle-selective optical transparency induced by photonic topological transition in Dirac semimetals-based hyperbolic metamaterials

QIN WANG,[1] LIWEI ZHANG,[2,*] XIAOLIN CAI,[1] PABLO CENCILLO-ABAD,[3] AND JUN-YU OU[4]

[1]School of Physics and Electronic Information Engineering, Henan Polytechnic University, Jiaozuo, Henan 454000, China
[2]School of Mathematics and Physics, Anqing Normal University, Anqing, Anhui 246133, China
[3]NanoScience Technology Center, University of Central Florida, Orlando, FL 32826, USA
[4]Optoelectronics Research Centre & Centre for Photonic Metamaterials, University of Southampton, Southampton, SO17 1BJ, United Kingdom
*zlwhpu@hotmail.com

Abstract: The tunable angle-selective transparency of hyperbolic metamaterials consisting of various multilayers of Dirac semimetal and dielectric materials are theoretically and numerically studied in the terahertz range. Three stack configurations are considered: alternating, sandwiched, and disordered. It is found that the proposed structures exhibit strong optical angular selectivity induced by photonic topological transition for transverse magnetic waves. Interestingly, the topological transition frequency can be flexibly modulated by changing the Fermi energy, temperature, and the releasing time of the Dirac semimetal, as well as the thickness ratio of the dielectric and semimetal layers. It is also noticed that the angular optical transparency properties are independent of the order of the proposed structure even in alternating/disordered/random configurations if the total thickness ratio of the semimetal to dielectric are the same, which makes the properties particularly easy to realize experimentally. The proposed hyperbolic metamaterial structures present a promising opportunity for wavefront engineering, offering crucial properties for applications in private screens, optical detectors, and light manipulation.

1. Introduction

Metamaterials, artificial media created by subwavelength structuring, have attracted great attention owing to their potential to manipulate electromagnetic waves. Over the past decades, metamaterials have been used to produce striking phenomena such as zero or negative refractive index, perfect absorption, or cloaking [1,2]. In recent years, among the many families of such structures, the family of hyperbolic metamaterials (HMMs) has attained substantial research interest [3–7]. In HMMs the electrical permittivity or magnetic permeability tensor component in one direction is opposite in sign to the other two principal components, thus presenting highly anisotropic characteristic that manifest in hyperbolic dispersion curves. Critically, to achieve these hyperbolic structures one only needs to constrain the motion of free electrons in one direction, making the fabrication of HMMs much simpler than that of isotropic metamaterials. Traditionally, HMMs in optical wavelengths have been produced by stacking multilayer metal/dielectric structures or embedding metal nanowires in a dielectric matrix [8,9]. However, for metals, inherent Joule losses are hard to overcome and modulating their permittivity challenging. These two factors greatly limit the preparation and application of metal-based HMMs. Graphene has been proposed as an alternative to metals. Graphene is a two-dimensional planar material composed of monolayer of carbon atoms with a singular electronic structure and unmatched

#458584 https://doi.org/10.1364/OE.458584
Journal © 2022 Received 17 Mar 2022; revised 18 May 2022; accepted 26 May 2022; published 9 Jun 2022

Optics EXPRESS

photoelectric properties. The greatest advantage of graphene, as compared to metals, is that its conductivity can be easily modulated by applying gate voltage, an electromagnetic field, or chemical doping [10]. Several HMMs based on graphene have been designed to obtain tunable optical properties [11–13]. Recently, a new kind of 3D materials, Dirac semimetals (DSs), have been reported. DSs have higher mobility than graphene, and their permittivity functions can also be dynamically modulated by changing their Fermi energy [14–16]. Furthermore, DSs are more stable and easier to fabricate than graphene, consequently, many tunable optical systems based on DSs, such as filters and absorbers, have been designed [17,18].

Recently, photonic topological transition (PTT) in metamaterials have attracted considerable research interest. PTT refers to the transition of the topology of the material's equifrequency surface from a closed to an open geometry. This transition provides an efficient method for the manipulation of the light-matter interactions at the nanoscale [19–23]. In particular, for anisotropic materials the topology transforms with the changing of the sign of one of the permittivity components. Thus, by modulating the topology of the equifrequency surface of the HMMs from a closed ellipsoid to an open hyperboloid, a narrow angular optical transparency window can be achieved around the PTT frequency [24]. Importantly, near the transition point of the equifrequency surface of the HMMs, the diffraction and scattering of the incident wave can be dramatically suppressed. This strong angle-selectivity makes the HMMs hold promise for many angle-dependent optical applications such as angular transparency. Not surprisingly, due to its practical applications in privacy screens and detectors, angular transparency has drawn many researchers' attention in recent years. Indeed, various methods and structures have been proposed to realize this goal, including photonic crystals, metallic gratings, and epsilon-near-zero media [25–30]. Su et al. realized a narrow angular optical transparency window using HMMs based on black phosphorus by PTT [31]. Using a HMM platform consisting of aligned metallic nanowires embedded in dielectric host matrices, Jiang et al. achieved tunable optical angular selectivity [32]. In a similar approach, Huo et.al. designed HMMs by filling silver nanowires in highly ordered porous anodic aluminum oxide templates and realized angular optical transparency based on PTT [33]. More recently, exploiting the naturally occurring anisotropy of hexagonal boron nitride, Wu reported a narrow angular optical transparency window near the four PTTs wavelengths [34].

In this work, we propose a HMMs based on DSs that enable tunable angular optical transparency induced by a photonic topological transition (PTT). The tunable angular optical transparencies occur at terahertz frequencies and are realized on a HMM structure composed of alternating dielectric and DSs. Transfer matrix method (TMM) [35] combined with effective medium theory (EMT) [36] and COMSOL simulations, are used to study their properties. Our calculations demonstrate transparency of almost 98% for transverse magnetic (TM) mode close to normal incidence with angular full width at half maximum of about 3°. Under the condition of keeping the total thickness ratio of the DS and dielectric material unchanged, the sequence of the multilayered structures can be alternating, sandwiched and disordered. Moreover, the proposed structures show wavevector selective effect [37], crucial in wavefront modulation applications. Interestingly, in contrast to previous designs, such as epsilon-near-zero media and hexagonal boron nitride [25,34], our proposed architecture offers a much narrower angle transparency window with a higher optical transparency. Additionally, the angular optical transparency can be actively adjusted by changing the Fermi energy of the DS, the temperature, and the releasing time of the DS in the Terahertz region. Furthermore, from an experimental point of view, the proposed scheme is fully compatible with conventional nanofabrication techniques such as molecular beam epitaxy [38] and chemical vapor deposition [39], making the DS-based HMM designs particularly suitable for experimental realization.

Optics EXPRESS

2. Structures and methodology

In this work we studied three multilayered structures composed of alternative layers of DS and dielectric material in three different configurations (I) alternating, (II) sandwiched, and (III) disordered. The three configurations are shown in Fig. 1, where A and B represent the DS and dielectric materials respectively. It should be noted that all three configurations maintain the same DS to dielectric thickness ratio. For the alternating arrangement, Fig. 1(a), the stack is composed of alternating A and B layers. For the sandwiched structure, shown in Fig. 1(b), the structure follows an "ACA" configuration, where the layer C is also a sandwiched structure: $C = BAB$. Finally, for the disordered arrangement, Fig. 1(c), where A and B layers are randomly arranged and the relative thickness deviations of the layer A and B are about 105% and 100%, respectively.

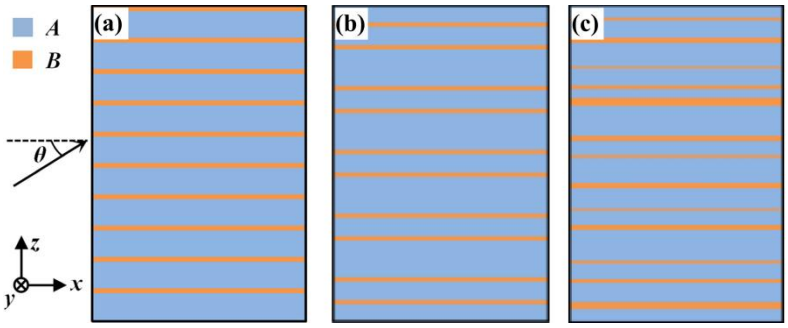

Fig. 1. Schematic of the proposed structures. (a) alternating structure(I) composed of alternating A and B layers. (b) Multilayered structure(II) with the "ACA" ($C = BAB$) sandwich structure as cells.(c) Disordered multilayered structure(III) randomly arranged by A and B layers.

We choose SiO_2 as the dielectric material A, with permittivity 2.25. On the other hand, DS is an optically isotropic material because of its 3D nature, whose permittivity can be deduced using the two-band model and taking into account the interband electronic transitions. In this manner, the permittivity of the DS is give by

$$\varepsilon = \varepsilon_\infty + i\sigma/\omega\varepsilon_0 \tag{1}$$

where ε_0 is the permittivity in vacuum and σ is the conductivity of the DS. ε_∞ is the effective background dielectric constant (for Na_3Bi or Cd_3As_2, $\varepsilon_\infty = 13$ [14–16]).

At the long-wavelength limit, the complex conductivity of the DS can be deduced using the Kubo formalism in the random phase approximation. Its real and imaginary part can be expressed as [14]

$$\mathrm{Re}\sigma(\Omega) = \frac{e^2}{\hbar}\frac{gk_F}{24\pi}\Omega G(\Omega/2) \tag{2}$$

$$\mathrm{Im}\sigma(\Omega) = \frac{e^2}{\hbar}\frac{gk_F}{24\pi^2}\left\{\frac{4}{\Omega}\left[1+\frac{\pi^2}{3}\left(\frac{T}{E_f}\right)^2\right] + 8\Omega\int_0^{\varepsilon_c}\left[\frac{G(\varepsilon)-G(\Omega/2)}{\Omega^2-4\varepsilon^2}\right]\varepsilon d\varepsilon\right\} \tag{3}$$

where, $\hbar$ is the reduced Planck constant, e is the charge of an electron, T is the temperature, and g is the degeneracy factor. The Fermi momentum is given by $k_F = E_f / \hbar v_F$, with f the frequency, and E_f and v_F the Fermi energy and velocity respectively. $\Omega = \hbar(2\pi f + i\tau^{-1})/E_f$ denotes the normalized frequency. $G(E) = n(-E) - n(E)$, with $n(E)$ being the Fermi distribution function, and $\varepsilon_c = E_c / E_f$ (E_c is the cutoff energy beyond which the Dirac spectrum is no longer linear). Here, we set $g = 4$ (for Na_3Bi or Cd_3As_2) [14], $\varepsilon_c = 3$, and $v_F = 10^6 m/s$. The electrical

Optics EXPRESS

permittivity can thus be obtained from formulas (1), (2) and (3), where is obvious that it can be tuned by adjusting the Fermi level, the temperature, and the releasing time.

For the composite structure, under the subwavelength limit, the DS-dielectric composite can be modeled as a homogeneous metamaterial. The effective medium theory (EMT) is valid to study the wave propagation in this periodic structure [36]. Therefore, in the following analysis, we use EMT and TMM to calculate the transmission properties of the multilayer structures. To further confirm the numerical results from TMM, we also compare with COMSOL simulations.

3. Results and discussion

3.1. Equifrequency surface and PTT in the proposed HMM structure (I)

The TM wave is incident on the structures from air at an incident angle θ with respect to the x axis, and is fully contained in the zx-plane. For the periodic structure I, the thicknesses of layers A and B are 1.8 μm and 0.2 μm respectively. The length of the structure in the x-direction is h. The effective relative permittivity tensor $[\varepsilon]$ is a diagonal matrix in Cartesian coordinates, without considering optical nonlocality under small incident angles [40]. When the incident wave propagates along the x-axis, the effective relative permittivity tensor can be expressed as:

$$\varepsilon = \begin{pmatrix} \varepsilon_{//} & 0 & 0 \\ 0 & \varepsilon_{//} & 0 \\ 0 & 0 & \varepsilon_{\perp} \end{pmatrix} \tag{4}$$

where, $\varepsilon_{//}$ and $\varepsilon_{\perp}$ denote the tangential and radial permittivity, respectively, which are approximated as follows [36]:

$$\varepsilon_{//} = \frac{\varepsilon_A d_A + \varepsilon_B d_B}{d_A + d_B}, \varepsilon_{\perp} = \frac{\varepsilon_A \varepsilon_B (d_A + d_B)}{\varepsilon_A d_B + \varepsilon_B d_A} \tag{5}$$

Hence, the dispersion equation of TM waves propagating inside our proposed HMM is given by:

$$\frac{k_x^2 + k_y^2}{\varepsilon_{\perp}} + \frac{k_z^2}{\varepsilon_{//}} = k_0^2 \tag{6}$$

where k_0 is the wave vector of the incident wave in the vacuum and k_x, k_y, and k_z are the components of the wave vector along the x-, y-, and z-directions respectively.

Formula (5) shows that the effective relative permittivity of the HMM is bound up with the permittivity of the DS and the thickness ratio of A to B once the dielectric B is selected. Figure 2(a) and (b) display the relationship between the real parts of the permittivity components $\varepsilon_{//}$ and $\varepsilon_{\perp}$(Re $-\ \varepsilon_{//}$ and Re $-\ \varepsilon_{\perp}$) and the thickness ratio of A to B. In Fig. 2(a), we can see that for a constant value of Re $-\ \varepsilon_{//}$, dotted lines overlaid, the frequency decreases with the increase of the thickness ratio of A to B, whereas for constant Re $-\ \varepsilon_{\perp}$, above thickness ratios A to B of 3, the frequency remains almost unchanged, see Fig. 2(b). The imaginary parts of $\varepsilon_{//}$ and $\varepsilon_{\perp}$ (Im $-\ \varepsilon_{//}$ and Im $-\ \varepsilon_{\perp}$), can be seen in Fig. 2(c) and (d). Overall the imaginary values are small, with Im $-\ \varepsilon_{//}$ decreasing with the increase of the thickness ratio of A to B, which shows the loss and absorption will be very small when the incident wave transmits through the HMM if the thickness ratios of A to B are set properly.

Figure 3(a) gives the permittivity of the HMM when the thickness ratio of A to B is 9:1. For this case it can be seen that Re $-\ \varepsilon_{//}$ of the HMM increases with frequency, while Re $-\ \varepsilon_{\perp}$ of the HMM is almost unchanged with frequency, and it is about 2.53. Re $-\ \varepsilon_{//}$ of the HMM is negative at low frequencies and when the frequency reaches 4.5019THz, it becomes zero. Once the frequency is above 4.5019 THz, Re $-\ \varepsilon_{//}$ of the HMM becomes positive. That is to say, Re $-\ \varepsilon_{//}$

Optics EXPRESS

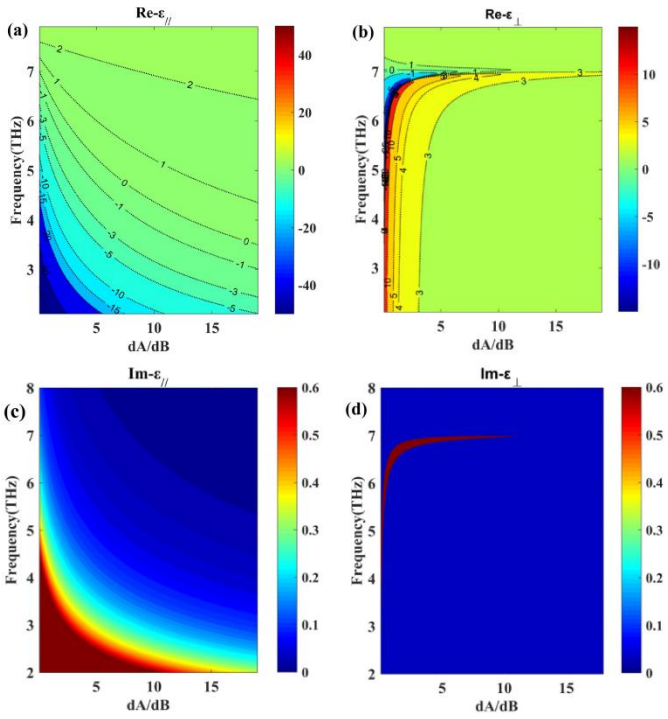

Fig. 2. The permittivity of the HMM as a function of frequency and thickness ratio of A to B. (a) Re $-\ \varepsilon_{//}$. (b) Re $-\ \varepsilon_{\perp}$. (c) Im $-\ \varepsilon_{//}$. (d) Im $-\ \varepsilon_{\perp}$. The dotted lines overlaid in (a) and (b) are constant real part lines.

of the HMM changes from negative value to positive value as the frequency increases. This means the dispersion of the HMM will change, and the topology of the equifrequency surface will transition from an open hyperbola to a closed ellipse as the frequency of the incident wave increases. This topological transition is indicative of the transition point of PTT. Specifically, the PTT occurs when Re $-\ \varepsilon_{//} = 0$, and the equifrequency surface degenerates, for lossless case, to two points in the x-direction. At this frequency, the HMM acts as a spatial frequency filter and only the TM waves with pure wavevector along x-axis are allowed to propagate thus producing an angular transparency window that only transmits light propagating along the x-axis. From Fig. 3(a), we can get a PTT frequency of 4.5019 THz. Combining with Fig. 2, adapting appropriate thickness ratio of the components of the HMM, we can get different PTT frequencies with high transmission.

When we set the thickness ratio of A to B to be 9:1, at the frequencies of 3.9609 THz, 4.4376 THz, 4.5019 THz, 4.5691 THz and 5.3494 THz, Re $-\ \varepsilon_{//}$ of the HMM takes the values Re $-\ \varepsilon_{//} = -1$, Re $-\ \varepsilon_{//} = -0.1$, Re $-\ \varepsilon_{//} = 0$, Re $-\ \varepsilon_{//} = 0.1$, and Re $-\ \varepsilon_{//} = 1$, respectively, while Re $-\ \varepsilon_{\perp}$ remains almost unchanged. Obtained from formula (5), we present the calculated k_x/k_0 of the HMM's equifrequency surface at the above five frequencies in Fig. 3(b) and (c). In Fig. 3(b) we present the real part of k_x/k_0 of the HMM's equifrequency surface. It can be clearly seen that while the equifrequency surface is an open hyperbola at the frequencies of 3.9609 THz and 4.4376 THz, it transitions to a closed ellipse at the frequencies of 4.5691 THz and 5.3494 THz. However, at frequency 4.5019 THz, the ellipse doesn't degenerate to two points at in the z-direction. Instead, at this frequency, the topology of the equifrequency surface keeps a very narrow hyperbola instead of the ideal degenerated point on the z-axis because of the imaginary part of $\varepsilon_{//}$ is not zero. Hence, compared to the ideal lossless medium, the lossy HMM allows TM

Optics EXPRESS

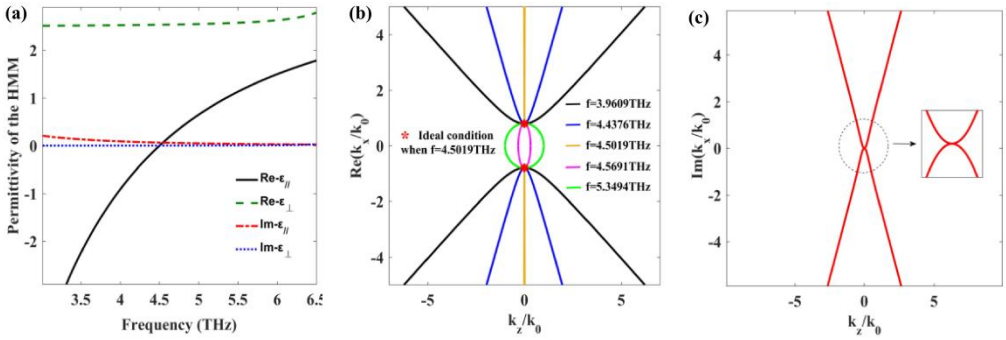

Fig. 3. (a) Permittivity of the HMM as a function of frequency with the thickness ratio of A to B being 9:1. (b) The real part of k_x/k_0 as a function of k_z/k_0 when the frequencies of the incident wave are 3.9609THz(Re-$\varepsilon_{//}$=-1), 4.4376THz(Re-$\varepsilon_{//}$=-0.1), 4.5019THz(Re-$\varepsilon_{//}$=0), 4.5691THz(Re-$\varepsilon_{//}$=0.1) and 5.3494THz(Re-$\varepsilon_{//}$=1), respectively. (c) The imaginary part of k_x/k_0 as a function of k_z/k_0 when the frequency of the incident wave is 4.5019THz(Re-$\varepsilon_{//}$=0). Here, we set other parameters as dA:dB = 9:1, T = 5 K, τ=2ps, and E_f = 0.08 eV.

waves with small k_z wavevectors to propagate. Furthermore, at the frequency of 4.5019 THz, the imaginary part of k_x/k_0 of the HMM's equifrequency surface exhibits a conical dispersion form with a Dirac-like point at the origin, as shown in Fig. 3(c). This means that for the TM waves with pure wavevectors along z-axis, the imaginary part of k_x is very close to zero, which indicates that the absorption losses have no influence on the incident wave at normal incidence. While the imaginary part of k_x increases rapidly with the incident angles. So the oblique incident wave will suffer from the intrinsic loss and the energy will be dissipated as the propagation distance increases. The existence of intrinsic loss makes it possible to suppress TM waves with large k_x, which is helpful in forming an ultra-narrow angular optical transparency window.

3.2. *Tunable PTT and angular transparency in the proposed HMM structure (I)*

From formulas (1), (2) and (3), we can see the Fermi energy of the DS, temperature, and the releasing time have an important effect on the permittivity of the DS, and thus can be used to modulate the PTT frequency. Figure 4(a) shows the relationship between Re $-\varepsilon_{//}$ of the HMM and the Fermi energy of the DS. Here, the thickness ratio of A to B is kept at 9:1. It is obvious that with the increase of the Fermi energy of the DS, the PTT frequency becomes larger. Hence, we can modulate the PTT frequency dynamically by adjusting the Fermi energy of the DS. Figure 4(b) shows Re $-\varepsilon_{//}$ of the HMM at different temperatures. It can be seen that the PTT frequency increases dramatically with temperature. Therefore, the PTT frequency can be adjusted flexibly by changing the temperature. Similarly, we analyze the effect of τ on the PTT frequency, as shown in Fig. 4(c). The PTT frequency has an obvious increasing when the τ is very small, while when τ is over 1ps, the increasing trend of the PTT frequency becomes gentle.

To gain further insight on the properties of the proposed HMM structure, we simulate their optical transmission. For the proposed HMM surrounded by the air, we provide the transmission as function of the incident angle and the thickness h along the x-axis of the HMM, as shown in Fig. 5(a). We can see that the transmission achieves maximum at thicknesses 20.95 μm, 41.94 μm, 62.87 μm and 83.77 μm at normal incidence, because these thicknesses satisfy the condition of transmission maximum [34], i.e., $h = mc/(2f\sqrt{\varepsilon_\perp})$ (where m is a non-zero positive integer and f is the frequency). Figure 5(b) gives the transmission curves where m is set to be 1, 4, and 16 at the PTT frequency of 4.5019 THz. We can see a narrow angular transparency window emerges. It is obvious that the thicker the HMM, the narrower the angular transparency window. This is because the intrinsic loss will increase with the increasing of the HMM's thickness, which

Optics EXPRESS

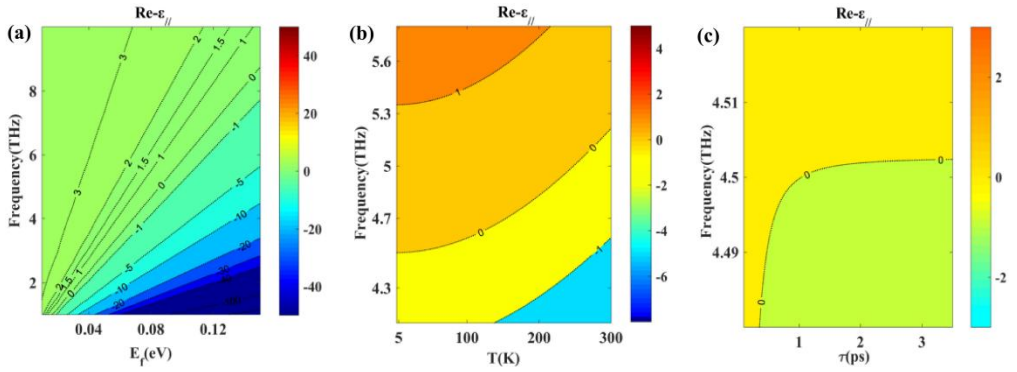

Fig. 4. (a) Re $-\varepsilon_{//}$ of the HMM as a function of frequency and Fermi energy, when dA:dB = 9:1, T = 5 K, and τ=2ps. (b) Re $-\varepsilon_{//}$ of the HMM as a function of frequency and temperature, when dA:dB = 9:1, $E_{\mathrm{f}} = 0.08$ eV, and τ=2ps. (c) Re $-\varepsilon_{//}$ of the HMM as a function of frequency and τ, when dA:dB = 9:1, T = 5 K, and $E_{\mathrm{f}} = 0.08$ eV.

will suppress the waves propagating away from x-direction. Figure 5(c) shows the transmission as a function of frequency and the incident angle when $m = 16$, and we can see at the optical transparency window appears at the frequency of 4.5019 THz, and the transparency window has an angular full width at half maximum of about 3° ($-1.6° < \theta < 1.6°$) with an optical transmission higher than 97.7% at normal incident. To ensure our numerical result, we simulate this result using COMSOL software combined with EMT. The comparison is shown in Fig. 5(d) where we can see the results are consistent.

At the same time, the electric field distributions along the x-axis in the air-HMM-air structure at the PTT frequency are provided to get a more intuitive understanding of the angular transparency features. Figure 5(e) and (f) show the electric field distributions at different incident angles of 0°, 1.6°, 3° and 5° calculated by TMM and EMT, as well as COMSOL and EMT, respectively. In the simulation using COMSOL, the light source is transverse magnetic plane wave, and Port Boundary Conditions are used. Floquet boundary conditions are adopted for the sides perpendicular to the propagation direction, and the meshing size is predefined "finer". It is obvious from this that both methods provide coincident results. At normal incidence, the incident wave travels smoothly in the HMM structure, almost lossless. However, the electric field in the HMM structure attenuates gradually as the incident angle increases, which means that the losses increase gradually. For instance, a wave incident at 1.6° will lose just about 50% of its amplitude as compared to the normal incidence case. As the incident angle further increases to 5°, most of the light is absorbed in the stack due to intrinsic losses and transmission approaches zero.

Next, the effect of the Fermi energy of the DS, temperature T, and the releasing time τ on the angle transparency are discussed. According to Fig. 3, with the increase of the E_f, temperature, and τ, the PPT frequency increases nearly linearly, rapidly, and gently, respectively. Figure 6(a) provides the transmission as a function of the incident angle and E_{f}, here τ=2 ps and T = 5 K. When E_{f} is set to 0.06 eV, 0.07 eV, 0.08 eV, and 0.09 eV, the PTT frequency changes to 3.3761 THz, 3.939 THz, 4.5019 THz and 5.0647 THz, respectively. That is, with 0.01 eV increase of E_{f}, the PPT frequency will increase about 0.55 THz. Meanwhile, the angle transparency property keeps almost unchanged at these different PTT frequencies. Figure 6(b) shows the transmission as a function of the incident angle and temperature, here $E_{\mathrm{f}} = 0.08$ eV and τ=2 ps. When the temperature changes from 5 K to 100 K, 200 K, and 300 K, the PTT frequency changes from 4.5019 THz to 4.5855THz, 4.8291THz and 5.2136THz, respectively. We can also see the transparency widow becoming a little narrower with the increase of temperature, although keeping the maximum of transmission almost unchanged. Figure 6(c) presents the transmission

Optics EXPRESS

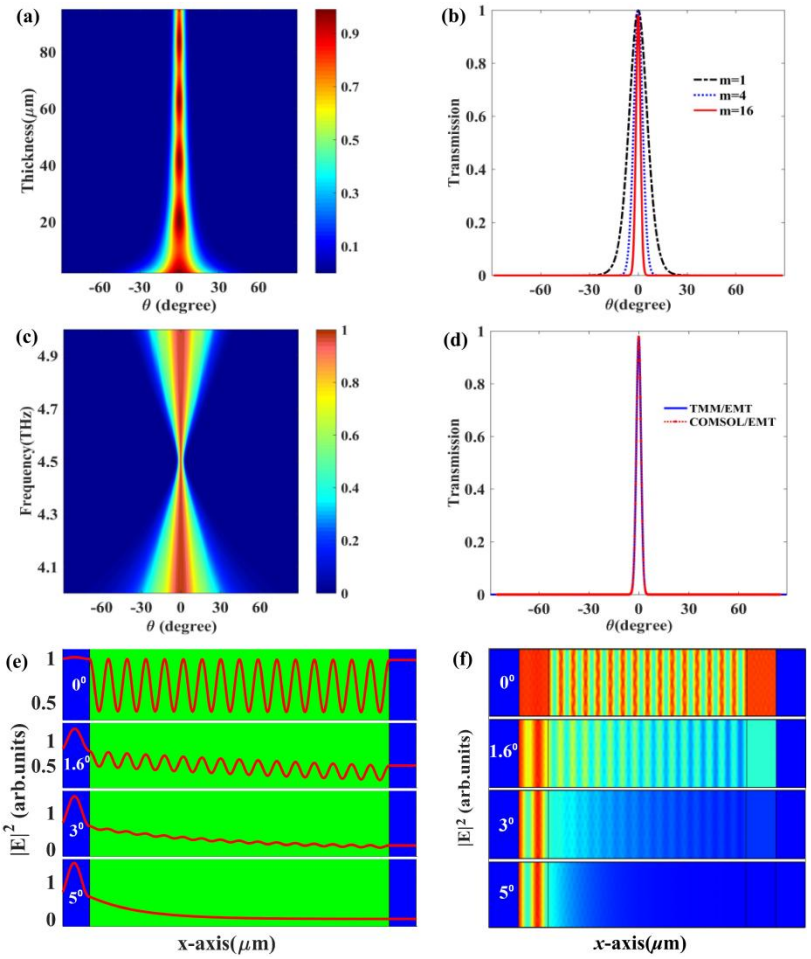

Fig. 5. (a) Transmission as function of thickness of the HMM along the x-axis and the incident angle at PPT frequency of 4.5019THz. (b) Transmission curves where $m = 1$, 4 and 16 at the PTT frequency of 4.5019THz. (c) Transmission as a function of frequency and the incident angle when $m = 16$. (d) TMM&EMT-calculated and COMSOL&EMT-simulated transmission as a function of incident angle at the PTT frequency of 4.5019THz, where $m = 16$. (e) Electric field distributions along the x-axis calculated using TMM&EMT. (f) Electric field distributions along the x-axis simulated by COMSOL&EMT. Here, we set other parameters as dA:dB = 9:1, $T = 5$ K, τ=2ps, and $E_f = 0.08$ eV.

Optics EXPRESS

as a function of the incident angle and τ, here $E_f = 0.08$ eV and T = 5 K. When τ increases from 0.45 ps to 1 ps, 2 ps, and 3 ps, the PTT frequency increases gently from 4.4887 THz to 4.4998 THz, 4.5019 THz, and 4.5023 THz, respectively. Additionally, the angular window of transparency becomes narrower with the increase of τ, also keeping the maximum of transmission almost unchanged. In consequence, a tunable angle transparency can be obtained by adjusting the Fermi energy level, changing the temperature, and the releasing time of the DSs.

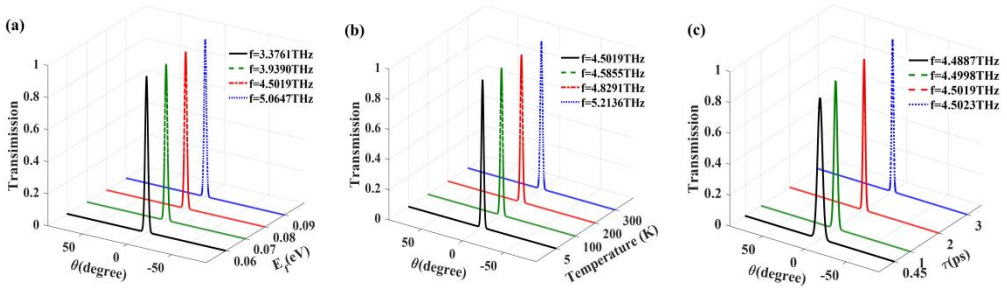

Fig. 6. (a) Transmission as a function of the incident angle at different Fermi energy, where T = 5 K and τ=2ps. (b) Transmission as a function of the incident angle at different temperature, where $E_f = 0.08$ eV and τ=2ps. (c) Transmission as a function of the incident angle at different τ, where $E_f = 0.08$ eV and T = 5 K.

3.3. *Angular transparency in the proposed HMM structures (II and III)*

Using COMSOL software, we also simulate the angular transparency properties in three configurations of the multilayered structure: (I) alternating, (II) sandwiched, and (III) disordered, as shown in Fig. 1. In the simulations, the sources and the boundary conditions are adopted the same with those set in Fig. 5(f). We find in this case that meshing size defined as "normal" offers a good balance between computational requirements and precision.

The transmission curves obtained from a TMM/EMT combination and COMSOL/EMT combination, as described before, are now compared to pure COMSOL simulations, see Fig. 7(a). The electric distributions in the air-structure (I)-air, air -structure (II)-air and air-structure (III)-air are also provided in Fig. 7(b), (c) and (d), respectively. From the comparison with the results calculated by TMM/EMT, it is seen that the results are very consistent. The properties of the angle transparency are almost unchanged, and all the transmissions at normal incidence remain above 97.7% (see the magnified detail in the inset of Fig. 7(a)). That is, the transmission characteristics are almost independent of the sequence of the layers. This indicates that under the condition of constant total thickness ratio of DS to dielectric material, the sequence of the multilayer structures can also have different periodicities or even total disordered without the loss of performance.

3.4. *Wavefront modulation of the HMM via angular transparency*

From Fig. 5(d), it is known that the proposed HMM structures present an ultra-narrow angular transparency performance close to normal incidence, where the equifrequency surface degenerates to two points at the lossless condition and the direction of wave propagation will be perpendicular to the equifrequency surface. Therefore, at the PTT frequency, the structure acts as a wavevector-selector metamaterial [37], that allows only plane waves with k-vectors parallel (or nearly parallel) to its normal, while absorbing or back-reflecting all other waves. Here, for the proposed HMM structures, we further explore the potential in application for wavefront engineering for the case of cylindrical-to-plane-wave conversion. In the simulation, we design an optical system in which a plane TM wave at normal incidence in air is projected on a copper plate with a narrow slit. The frequency of the incident wave is 4.5019 THz (wavelength is about 66.64 μm), and the

Optics EXPRESS

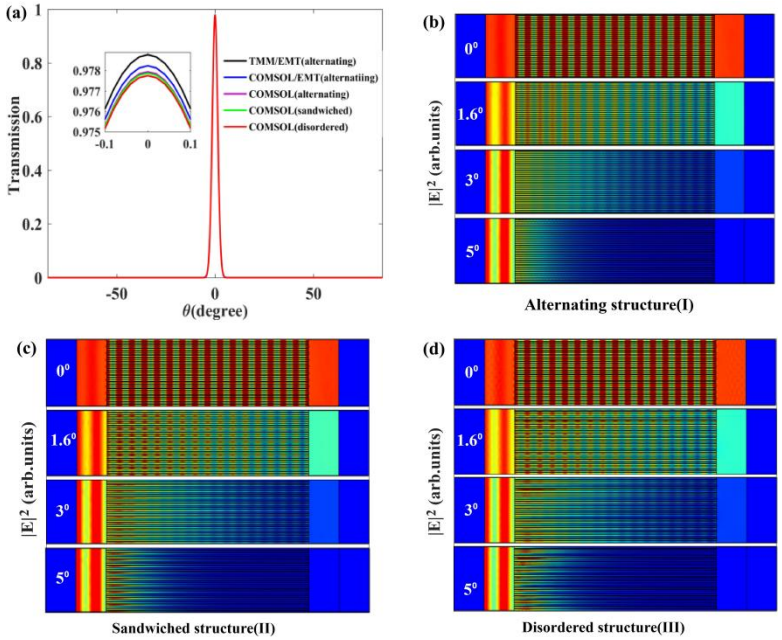

Fig. 7. (a) Transmission as a function of the incident angle from a TMM/EMT combination, COMSOL/EMT combination and pure COMSOL simulation in the proposed structures (inset: the magnified detail figure). (b), (c) and (d) are electric field distributions along x-axis in alternating structure, sandwiched structure and disordered structure, respectively. Here we set other parameters as T = 5 K, E_f = 0.08 eV, and τ=2ps.

thickness of the plate and the width of the slit are 20 μm and 60 μm, respectively. The electric field distributions along the x-axis are simulated using COMSOL software. In the simulation, perfectly matched layers are assigned at all the surrounding boundaries, and the meshing size is predefined "finer".

A line-divergent wave scattered in wide directions can be produced by launching a plane wave from air to a copper plate with a narrow subwavelength slit, Fig. 8(a). However, immediately after the slit we place the proposed HMM structure, the scattered wave transmits smoothly and the propagated wavefronts appear parallel to the plane of the HMM, Fig. 8(b). It is important to notice that the obtained parallel light mechanism is different from that of a conventional lens. In addition, by changing the slit width, we find that this effect does not depend on the curvature of the incident wavefronts. In other words, our proposed HMM structure provides a new degree of freedom for light manipulation. Indeed, as the HMM is transparent only within a narrow range of light propagation directions at PTT frequency, arbitrary-shaped wavefronts will become planar as they transmit through the HMM plane without any additional spatial phase modulation. The schematic of this wavefront conversion process is shown in the inset of Fig. 8(c). For a beam of cylindrical-like wave excited by a copper slit located at about 200 μm from the HMM, with thicknesses of the slit and the HMM plane being 20 μm and 80 μm respectively, the simulated electric field distribution are shown in Fig. 8(c), offering further evidence that, as expected, the cylindrical-like wave can be converted into a plane wave by the HMM.

Optics EXPRESS

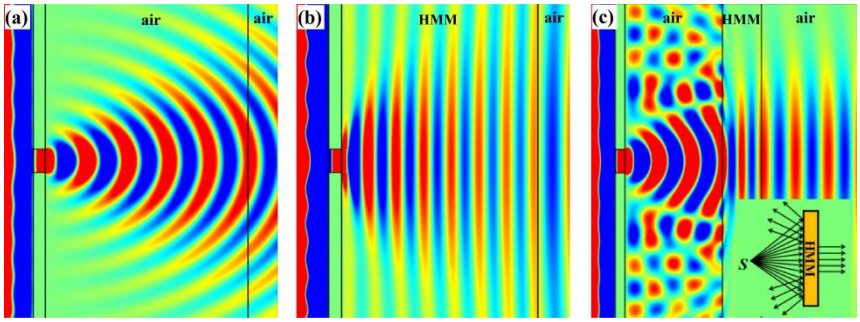

Fig. 8. The electric field distributions after the plane TM waves incident vertically to a slit in a copper plate, where dA:dB = 9:1, T = 5 K, E_f = 0.08 eV, and τ=2ps. (a)The TM waves transmit in air. (b)The TM waves pass through the proposed HMM structure. The width of the slit is 60μm, and thickness of the copper plane is 20μm. (c) Electric feld distribution of the wavefront conversion (The inset is the schematic of the wavefront conversion process).

4. Conclusions

In this work, we proposed HMM structures consisting of multilayered DS and dielectric material. The numerical results show that the designed structures exhibit strong optical angular selectivity for TM waves. Based on PTT, at terahertz frequencies, a tunable ultra-narrow ($-1.6° < \theta < 1.6°$) angular optical transparency window can be obtained. Importantly, this band offers ultra-high transparency (over 97.7%) for near-incidence illumination. Furthermore, the PTT frequency can be dynamically modulated by adjusting the Fermi energy of the DS, the temperature, or the releasing time of the DS, as well as by changing the thickness ratio of DS to dielectric material. Interestingly, this optical angular selectivity can be maintained in different periodicities and even completely disordered structures, provided that the total material thickness ratio is maintained, making the stack structure particularly suitable for experimental realization. Critically, the proposed HMM structure presents a marked wavevector-selective effect, that can be used in wavefront modulation, presenting an exciting opportunity for applications such as private screens, optical detectors, and wavefront engineering.

Funding. Natural Science Foundation of Anhui Higher Education Institutions of China (KJ2020A0504); National Natural Science Foundation of China (11804082, U1804165); Foundation of Henan Educational Committee (18A140018).

Disclosures. The authors declare no conflicts of interest.

Data availability. Data underlying the results presented in this paper are not publicly available at this time but may be obtained from the authors upon reasonable request.

References

1. Y. Yao, Z. F. Liao, Z. Q. Liu, X. S. Liu, J. Zhou, G. Q. Liu, Z. Yi, and J. Q. Wang, "Recent progresses on metamaterials for optical absorption and sensing: a review," J. Phys. D: Appl. Phys. **54**(11), 113002 (2021).
2. D. Zhao, Z. L. Lin, W. Q. Zhu, H. J. Lezec, T. Xu, A. Agrawal, C. Zhang, and K. Huang, "Recent advances in ultraviolet nanophotonics: from plasmonics and metamaterials to metasurfaces," Nanophotonics **10**(9), 2283–2308 (2021).
3. S. V. Zhukovsky, O. Kidwai, and J. E. Sipe, "Physical nature of volume plasmon polaritons in hyperbolic metamaterials," Opt. Express **21**(12), 14982–14987 (2013).
4. P. C. Huo, S. Zhang, Y. Z. Liang, Y. Q. Lu, and T. Xu, "Hyperbolic Metamaterials and Metasurfaces: Fundamentals and Applications," Adv. Opt. Mater. **7**(14), 1801616 (2019).
5. Y. R. He, S. L. He, J. Gao, and X. D. Yang, "Giant transverse optical forces in nanoscale slot waveguides of hyperbolic metamaterials," Opt. Express **20**(20), 22372–22382 (2012).
6. P. Ginzburg, A. V. Krasavin, A. N. Poddubny, P. A. Belov, Y. S. Kivshar, and A. V. Zayats, "Self-induced torque in hyperbolic metamaterials," Phys. Rev. Lett. **111**(3), 036804 (2013).
7. D. Lu, J. J. Kan, E. E. Fullerton, and Z. W. Liu, "Enhancing spontaneous emission rates of molecules using nanopatterned multilayer hyperbolic metamaterials," Nat. Nanotechnol. **9**(1), 48–53 (2014).

Optics EXPRESS

8. B. Wood, J. B. Pendry, and D. P. Tsai, "Directed subwavelength imaging using a layered metal-dielectric system," Phys. Rev. B **74**(11), 115116 (2006).
9. R. Kotynski and T. Stefaniuk, "Multiscale analysis of subwavelength imaging with metal-dielectric multilayers," Opt. Lett. **35**(8), 1133–1135 (2010).
10. S. K. Tiwari, S. Sahoo, N. Wang, and A. Huczko, "Graphene research and their outputs: Status and prospect," J. Sci.: Adv. Mater. Devices **5**(1), 10–29 (2020).
11. Z. P. Su and Y. K. Wang, "Dynamically tunable angular optical transparency induced by photonic topological transition in graphene-based hyperbolic metamaterials," Opt. Mater. **107**, 110074 (2020).
12. P. Sun, C. L. You, A. Mahigir, T. T. Liu, F. Xia, W. J. Kong, G. Veronis, J. P. Dowling, L. F. Dong, and M. J. Yun, "Graphene-based dual-band independently tunable infrared absorber," Nanoscale **10**(33), 15564–15570 (2018).
13. X. Wang, X. Jiang, Q. You, J. Guo, X. Y. Dai, and Y. J. Xiang, "Tunable and multichannel terahertz perfect absorber due to Tamm surface plasmons with graphene," Photonics Res. **5**(6), 536–542 (2017).
14. O. V. Kotov and Y. E. Lozovik, "Dielectric response and novel electromagnetic modes in three-dimensional Dirac semimetal films," Phys. Rev. B **93**(23), 235417 (2016).
15. Z. K. Liu, B. Zhou, Y. Zhang, Z. J. Wang, H. M. Weng, D. Prabhakaran, S. K. Mo, Z. X. Shen, Z. Fang, X. Dai, Z. Hussain, and Y. L. Chen, "Discovery of a Three-Dimensional Topological Dirac Semimetal, Na3Bi," Science **343**(6173), 864–867 (2014).
16. Z. K. Liu, J. Jiang, B. Zhou, Z. J. Wang, Y. Zhang, H. M. Weng, D. Prabhakaran, S. K. Mo, H. Peng, P. Dudin, T. Kim, M. Hoesch, Z. Fang, X. Dai, Z. X. Shen, D. L. Feng, Z. Hussain, and Y. L. Chen, "A stable three-dimensional topological Dirac semimetal Cd3As2," Nat. Mater. **13**(7), 677–681 (2014).
17. G. D. Liu, X. Zhai, H. Y. Meng, Q. Lin, Y. Huang, C. J. Zhao, and L. L. Wang, "Dirac semimetals based tunable narrowband absorber at terahertz frequencies," Opt. Express **26**(9), 11471–11480 (2018).
18. Q. Wang and L. W. Zhang, "Tunable narrow terahertz absorption of one-dimensional photonic crystals embedded with Dirac semimetal–dielectric defect layers," Appl. Opt. **58**(31), 8486–8494 (2019).
19. L. Lu, J. D. Joannopoulos, and M. Soljacic, "Topological photonics," Nat. Photonics **8**(11), 821–829 (2014).
20. H. N. S. Krishnamoorthy, Z. Jacob, E. Narimanov, I. Kretzschmar, and V. M. Menon, "Topological Transitions in Metamaterials," Science **336**(6078), 205–209 (2012).
21. A. V. Shchelokova, D. S. Filonov, P. V. Kapitanova, and P. A. Belov, "Magnetic topological transition in transmission line metamaterials," Phys. Rev. B **90**(11), 115155 (2014).
22. J. S. Gomez-Diaz, M. Tymchenko, and A. Alu, "Hyperbolic Plasmons and Topological Transitions Over Uniaxial Metasurfaces," Phys. Rev. Lett. **114**(23), 233901 (2015).
23. W. L. Gao, M. Lawrence, B. Yang, F. Liu, F. Z. Fang, B. Beri, J. S. Li, and S. Zhang, "Topological Photonic Phase in Chiral Hyperbolic Metamaterials," Phys. Rev. Lett. **114**(3), 037402 (2015).
24. X. Y. Wang, T. Wang, Q. F. Zhong, R. Q. Yan, and X. Hang, "Ultrabroadband light absorption based on photonic topological transitions in hyperbolic metamaterials," Opt. Express **28**(1), 705–714 (2020).
25. L. V. Alekseyev, E. E. Narimanov, T. Tumkur, H. Li, Y. A. Barnakov, and M. A. Noginov, "Uniaxial epsilon-near-zero metamaterial for angular filtering and polarization control," Appl. Phys. Lett. **97**(13), 131107 (2010).
26. Q. Y. Qian, C. Q. Xu, and C. H. Wang, "All-dielectric polarization independent optical angular filter," Sci. Rep. **7**(1), 16574 (2017).
27. C. Q. Xu, A. A. Fang, H. C. Chu, J. Luo, C. T. Chan, Z. H. Hang, and Y. Lai, "Angular selection of incident waves by photonic crystals with position-varying Dirac points at the Brillouin zone boundary," Phys. Rev. B **93**(24), 245116 (2016).
28. Y. D. Lu, L. S. Yan, Y. H. Guo, Y. Pan, W. Pan, and B. Luo, "Elevation-azimuth angular selectivity and angle-frequency filtering in asymmetric photonic crystal," Opt. Express **24**(21), 24473 (2016).
29. J. Y. Guo, S. F. Chen, and S. J. Jiang, "Optical broadband angular filters based on staggered photonic structures," J. Mod. Opt. **65**(8), 928–936 (2018).
30. Y. C. Shen, D. X. Ye, I. Celanovic, S. G. Johnson, J. D. Joannopoulos, and M. Soljacic, "Optical Broadband Angular Selectivity," Science **343**(6178), 1499–1501 (2014).
31. Z. P. Su and Y. K. Wang, "Anisotropic Photonics Topological Transition in Hyperbolic Metamaterials Based on Black Phosphorus," Nanomaterials **10**(9), 1694 (2020).
32. X. Y. Jiang, T. Wang, L. Cheng, Q. F. Zhong, R. Q. Yan, and X. Huang, "Tunable optical angular selectivity in hyperbolic metamaterial via photonic topological transitions," Opt. Express **25**(22), 27028–27036 (2017).
33. P. C. Huo, Y. Z. Liang, S. Zhang, Y. Q. Lu, and T. Xu, "Angular Optical Transparency Induced by Photonic Topological Transitions in Metamaterials," Laser Photonics Rev. **12**(8), 1700309 (2018).
34. X. H. Wu, "Angular optical transparency induced by photonic topological transition in hexagonal boron nitride," Plasmonics **14**(4), 973–977 (2019).
35. L. W. Zhang, W. Y. Yu, J. Y. Ou, Q. Wang, X. L. Cai, B. J. Wang, X. H. Li, R. Q. Zhao, and Y. J. Liu, "Midinfrared one-dimensional photonic crystal constructed from two-dimensional electride material," Phys. Rev. B **98**(7), 075434 (2018).
36. O. Kidwai, S. V. Zhukovsky, and J. E. Sipe, "Effective-medium approach to planar multilayer hyperbolic metamaterials: Strengths and limitations," Phys. Rev. A **85**(5), 053842 (2012).
37. V. A. Fedotov, J. Wallauer, M. Walther, M. Perino, N. Papasimakis, and N. I. Zheludev, "Wavevector Selective Metasurfaces and Tunnel Vision Filters," Light: Sci. Appl. **4**(7), e306 (2015).

Optics EXPRESS

38. Y. F. Meng, C. H. Zhu, Y. Li, X. Yuan, F. X. Xiu, Y. Shi, Y. B. Xu, and F. Q. Wang, "Three-dimensional Dirac semimetal thin-film absorber for broadband pulse generation in the near-infrared," Opt. Lett. **43**(7), 1503–1506 (2018).
39. Y. Cheng, K. Wang, Y. Qi, and Z. F. Liu, "Chemical vapor deposition method for graphene fiber materials," *Wuli Huaxue Xuebao* 2006046 (2020).
40. L. Sun, Z. G. Li, T. S. Luk, X. D. Yang, and J. Gao, "Nonlocal effective medium analysis in symmetric metal-dielectric multilayer metamaterials," Phys. Rev. B **91**(19), 195147 (2015).